Article

Flowering Poration—A Synergistic Multi-Mode Antibacterial Mechanism by a Bacteriocin Fold

multi-helix bacteriocin

induces multi-mode membrane poration

100 nm

each two-helix segment induces a particular mode

500 nm

α1α2   α2α3   α3α4

Katharine Hammond, Helen Lewis, Samantha Halliwell, ..., Mathew Upton, Jeremy P. Derrick, Maxim G. Ryadnov

max.ryadnov@npl.co.uk

HIGHLIGHTS

Bacteriocins are antibacterial proteins believed to form pores in bacterial membranes

A multi-helix bacteriocin fold induces a multi-mode poration mechanism

Each of two-helix segments of the bacteriocin adopts a particular poration mode

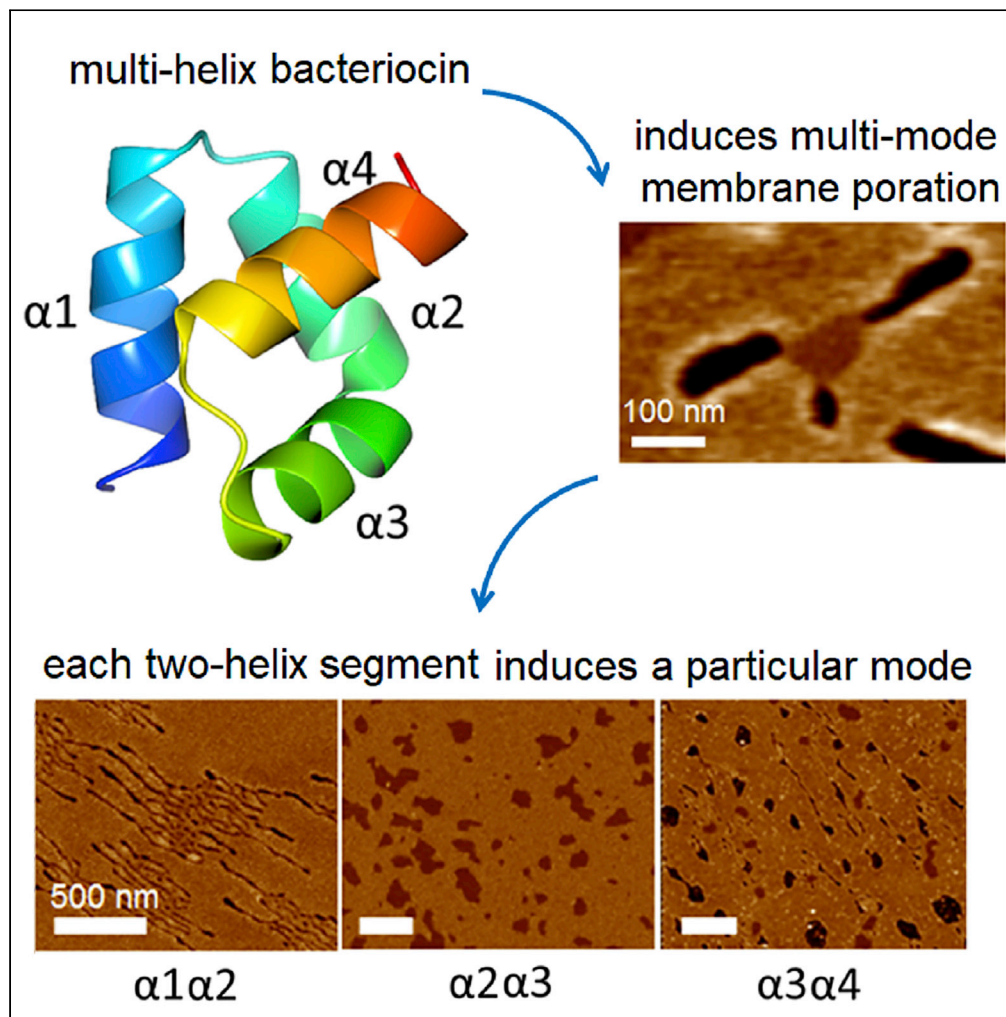These segments act synergistically balancing out antibacterial and hemolytic activities

Article

Flowering Poration—A Synergistic Multi-Mode Antibacterial Mechanism by a Bacteriocin Fold

Katharine Hammond,[1,2,3] Helen Lewis,[1] Samantha Halliwell,[4] Florie Desriac,[5] Brunello Nardone,[1] Jascindra Ravi,[1] Bart W. Hoogenboom,[2,3] Mathew Upton,[5] Jeremy P. Derrick,[4] and Maxim G. Ryadnov[1,6,7,*]

SUMMARY

Bacteriocins are a distinct family of antimicrobial proteins postulated to porate bacterial membranes. However, direct experimental evidence of pore formation by these proteins is lacking. Here we report a multi-mode poration mechanism induced by four-helix bacteriocins, epidermicin NI01 and aureocin A53. Using a combination of crystallography, spectroscopy, bioassays, and nanoscale imaging, we established that individual two-helix segments of epidermicin retain antibacterial activity but each of these segments adopts a particular poration mode. In the intact protein these segments act synergistically to balance out antibacterial and hemolytic activities. The study sets a precedent of multi-mode membrane disruption advancing the current understanding of structure-activity relationships in pore-forming proteins.

INTRODUCTION

Host defense systems use pore-forming proteins to target pathogenic, host, or aberrant cells (Parker and Feil, 2005). Bacteria secrete such proteins to access nutrients from the cells of their hosts or outcompete other bacteria living in the same environmental niches (Koehbach and Craik, 2019; Cotter et al., 2013), whereas human leukocytes release pore-forming proteins to kill pathogens (Iacovach et al., 2010). The spread of antimicrobial resistance has intensified interest in molecules promoting the lysis of microbial membranes with an emphasis on host defense peptides as potential anti-infectives (Lazar et al., 2018). These peptides favor attack on microbial membranes, and each tends to support one poration mechanism. The adoption of different mechanisms within the same sequence can be tuned by careful site-directed mutations (Pfeil et al., 2018). This modulation is possible because host defense peptides adopt relatively simple conformations in membranes. For example, only a single, short helix is required to elicit strong antimicrobial effects (Koehbach and Craik, 2019). Bacteria themselves produce more complex antibacterial agents, termed bacteriocins, which specialize in killing closely related bacterial strains (Acedo et al., 2018). The killing is proposed to occur through membrane poration, although experimental evidence for this conjecture has yet to be reported (Hechard and Sahl, 2002).

Bacteriocins can be divided into subclasses according to their structural organization and size (Arnison et al., 2013), with the most recent subclass represented by a multi-helix bundle group. Bacteriocins of this subclass are small proteins comprising several α helices packed into compact globular structures. Unlike other bacteriocins that have post-translational backbone or side-chain modifications or operate as tertiary complexes, proteins from this subclass are leaderless, single chain, and cysteine-free (Cotter et al., 2005, 2013).

Given that their structures are multi-helix folds, we reason that these proteins must induce multi-mode mechanisms of membrane disruption, with each mode supported by a specific constituent of their structure. Herein we validate this hypothesis, reporting the direct observation of multi-mode membrane disruption by bacteriocins. We first determine a high-resolution crystal structure of epidermicin NI01, a four-helix bacteriocin recently discovered in *S. epidermis* (Figure 1A) (Sandiford and Upton, 2012). We then synthesize individual constituents of this structure—two- and three-helix hairpins (Figures 1A and S1 in Supplemental Information)—characterize their biological and physical properties, and compare them with those of the full-length epidermicin. Using atomic force microscopy, we demonstrate that each of helix-helix hairpins induces a distinct mode of membrane disruption in anionic phospholipid bilayers, whereas the intact protein combines all these modes into one synergetic mechanism which, to our knowledge, has not been observed before. We further demonstrate that this mechanism is not stereoselective as it is reproduced by

Figure 1. The Structure of NI01

(A) Primary structure of NI01 and its derivatives—two-helix and three-helix hairpins, and an arginine mutant, R-NI01. Colored staples indicate π-π interactions between aromatic residues of different helices, labeled α1-α4. Turns are underlined in the sequences. Arginine residues in R-NI01 are shown in blue.

(B) Crystal structure of NI01. Ribbon representation from the N terminus (blue) to the C terminus (red).

(C) Stick representation of the central kink linking two terminal hairpins at H25.

(D) Two aromatic pairs, F4-W23 and W32-W41, between sequential helices: α1α2 and α3α4, respectively.

(E) Remaining three aromatic pairs, all involving the C-terminal helix, H25-W50, Y18-Y43, and F10-F39.

the all-D version of NI01. We show that all tested structures are appreciably antimicrobial and that synergy between the different corresponding modes of membrane disruption balances out the antibacterial and hemolytic activities of the protein. Finally, we compare the disruption mechanisms of NI01 and another bacteriocin from the same fold group and find that the two mechanisms are strikingly similar sharing the same disruption modes.

RESULTS

NI01 Folds into a Four-Helix Bundle Topology

The X-ray structure of NI01 revealed that it folds into a compact, four-helix bundle in which two α hairpins are linked through a kink ($\varphi = -116°$ and $\psi = 36°$) in the central helix at H25 (Figures 1B and 1C).
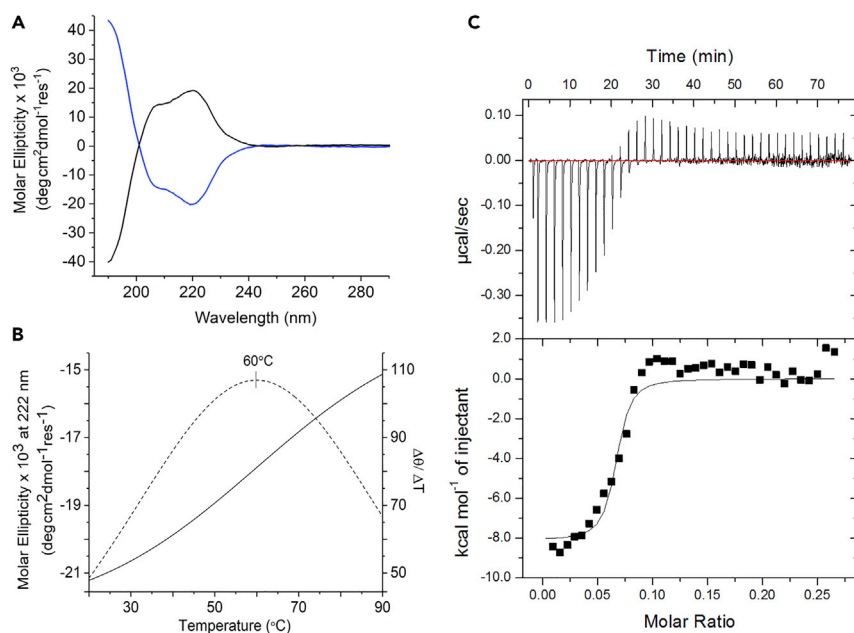
Figure 2. NI01 Folding

(A) CD spectra for NI01 (blue line) and its all-D form (20 μM protein) in 10 mM phosphate buffer (black line).

(B) Thermal unfolding curve and its first derivative highlighting a single transition point (T_M).

(C) Isothermal titration calorimetry of NI01 (500 μM) binding to bacterial mimetic membranes. Heat absorbed (μcal/s) for each isotherm is plotted versus titration time (upper panel). Integrated heats (kcal/mol) are plotted versus protein-lipid molar ratios (lower panel), showing a curve fitting to a one-set binding model (black line).

The transition between α1 and α2 is mediated by a type III β turn, and from α3 to α4 by G36, which forms a break at the end of the third helix (Figure 1B and Table S1). The hydrophobic residues of all helices are buried in the core of the bundle, which is characteristic of bacteriocins and essential to stabilize the fold in solution. Aromatic residues account for 20% of all residues in this protein but are not engaged in the core. Instead, their side chains are locked in paired π-π interactions that appear to act as staples between spatially adjacent helices. Five pairs are formed to support inter-helical crossovers, only two of which are formed between sequential helices, namely, the F4-W23 and W32-W41 pairs that link α1 and α2, and α3 and α4 helices, respectively (Figure 1D). Four of the pairs involve the C-terminal helix (α4) including all of the remaining pairs, H25-W50, Y18-Y43, and F10-F39 (Figure 1E). Given that this helix is stapled with each of the other three helices, it may function as a leader helix, which synchronizes the insertion of NI01 into membranes. The central α2 and α3 helices share no aromatic pairs between them, which is expected for helices oriented perpendicular to one another, and is common for leaderless bacteriocins (Lohans et al., 2013). Finally, the analysis of the structure by PISA (Krissinel and Henrick, 2007) did not indicate any significant contacts between protein monomers indicating that the protein is monomeric in aqueous solution (Figure 1B).

NI01 Folds Cooperatively in Solution and Binds Strongly to Anionic Membranes

Each helix in NI01 is at least two helical turns in length, which is sufficient to support the cooperative folding of the protein. Circular dichroism (CD) spectroscopy confirmed helix formation by NI01 in aqueous buffers (Figure 2A), with sigmoidal unfolding curves giving a single transition midpoint (T_M) of ∼60°C (Figure 2B).

Denaturation was also fully reversible: the spectra collected before and after the thermal denaturation were nearly identical (Figure S2A). The signal intensity at 202 nm, which remained the same during denaturation provided a clear isodichroic point indicating a two-state transition between helical and unfolded forms (Figure S2B). However, even at temperatures as high as 90°C NI01 retained helical content: the spectral $\Delta\varepsilon_{222}/\Delta\varepsilon_{208}$ ratios for all spectra recorded during the thermal transition were ≥1, as expected for helical bundles (Figures 2A and S2B) (Kelly et al., 2005). The observation is consistent with the fact that NI01 retains antimicrobial activity following exposure to elevated temperatures (80°C), as reported elsewhere (Arnison

et al., 2013). The helical content of the protein in aqueous buffers was comparable with that in aqueous 2,2,2-trifluoroethanol (TFE) (Figure S2C). Fluorinated alcohols promote intramolecular hydrogen bonding by excluding water from the solute and encompassing the polypeptide chain in a hydrophobic "matrix" (Roccatano et al., 2002). Thus, the TFE-induced helix formation shows the extent to which an individual chain can fold into a helical state excluding supramolecular contributions. With no apparent changes at different TFE concentrations (Figure S2C), the helical content of NI01 was also independent of peptide concentrations (Figure S2D). Collectively, the results are indicative of a highly stable protein that is fully folded in solution.

Similar to other pore-forming proteins, which target bacteria, epidermicin is cationic having a net charge of +8 at neutral pH. In the crystal structure of NI01, polar side chains of each helix cluster on the exterior of the protein. In solution, the protein is a monodisperse particle of 2 nm in diameter exhibiting a high surface charge (ζ-potential of 20.8 $\pm$ 3.8 mV). These characteristics confer a high stability on the protein, allowing it to bind to anionic bacterial membranes as a monomer (Figure S3). Since NI01 is already folded in solution, CD spectroscopy could only reveal additive changes in helicity in membranes. As expected, the helical content for NI01 remained unchanged when it was measured in reconstituted phospholipid bilayers, which were constructed as unilamellar vesicles to mimic bacterial (anionic) and mammalian (zwitterionic) membranes (Figure S4A). Isothermal titration calorimetry (ITC) provided a more quantitative measure of protein-membrane interactions. Measured by titrating NI01 into anionic phospholipid membranes, binding isotherms revealed an exothermic process indicating enthalpy-driven ionic and hydrogen-bond interactions (Figure 2C). As protein-lipid ratios increased endothermic processes became more pronounced suggesting increasing contributions from hydrophobic interactions. This can be attributed to that the protein inserts deep into the hydrophobic interface of the bilayer (Figure 2C). The integrated heats fitted into a single site binding model gave a dissociation constant (K_D) of 0.3 μM with a ΔG of -8.9 kcal/mol, both values consistent with the characteristics of membrane-targeting antibiotics and pore-forming proteins (Seelig, 2004; Khatib et al., 2016). The biphasic binding found during the titrations suggests a synergistic, multi-mode mechanism by which NI01 selectively targets bacterial membranes. No binding was detected in zwitterionic phospholipid membranes (Figure S4B), consistent with negligible levels of toxicity toward mammalian cells lines (Sandiford and Upton, 2012) and erythrocytes (Table S2). It can thus be concluded that the protein selectively disrupts bacterial membranes by binding to their surfaces through charge interactions and then re-arrangement into pores or channels.

NI01 Induces a Synergistic, Multi-Mode Poration Mechanism in Anionic Membranes

We probed the mechanism of membrane disruption by visualizing the effect of NI01 on reconstituted membranes using time-resolved atomic force microscopy in aqueous buffers (in-liquid AFM). The membranes of the same lipid composition used for the biophysical measurements in solution were deposited on mica surfaces as supported lipid bilayers (SLBs) (Rakowska et al., 2013). The resulting preparations yield flat (to within ≤0.1 nm) fluid-phase membranes that allow for accurate depth measurements of surface changes (Lin et al., 2006; Mingeot-Leclercq et al., 2008). Within minutes NI01 formed floral patterns on the SLBs. These patterns comprised roughly circular patches of thinned membranes radially propagating with petal-like lesions or pores (Figures 3A and S5A). Most patterns had three petals per patch (Figure 3B). The patches were ∼2 nm in depth half-way through the bilayer, which is consistent with membrane thinning effects commonly observed for antimicrobial peptides (Pfeil et al., 2018). In contrast, the petal-like lesions extended all the way across the membrane (4 nm), i.e., were transmembrane pores (Figure 3C). The lesions were tapered at one end connecting with their respective patches, whereas the opposite end appeared as a growing circular pore merging with other pores (Figures 3D, 3E, and S5A). Complementary to the ITC results, the AFM measurements showed that the bacteriocin was selective toward bacterial membranes. No changes could be detected in SLBs mimicking mammalian membranes, even at higher concentrations (Figure S5B).

The patches of thinned membranes appear as contact regions from which NI01 radially diffuses into the lipid matrix. This scenario resembles mechanisms proposed for four- and five-helix protein toxins that insert into the upper leaflet of the bilayer where they arrange into pores (González et al., 2000; Michalek et al., 2013). Similarly, antimicrobial peptides accumulate in the upper leaflet causing the thinning of phospholipid bilayers (Heath et al., 2018). These studies indicate that as more peptide binds to the bilayers thinning areas grow in size but not in depth, as also observed for NI01 (Figure 3E) (Mecke et al., 2005). This
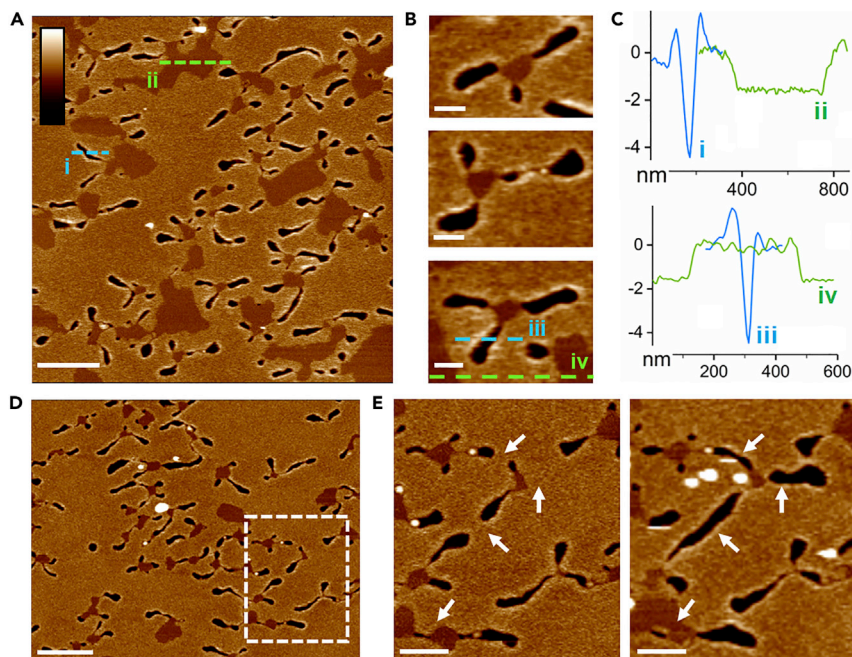
Figure 3. In Liquid AFM Imaging of Reconstituted Bacterial Membranes Incubated with NI01

(A) Topography of NI01-treated SLBs mimicking bacterial membranes (see Methods).

(B) Higher magnification images of individual patches (brighter areas) with petal-like pores (darker areas) from (A). The images were taken within the first 10 min of incubation with NI01 (0.25 μM).

(C) Height profiles as measured along the highlighted lines in (A) and (B).

(D and E) (D) SLBs imaged at a low magnification, with the framed area imaged at a higher magnification (E) over 1 h to show growing pores and patches as highlighted by white arrows (from left to right). Color scale bar is 15 nm. Length scale bars are 500 nm for (A) and (D), 100 nm for (B), and 200 nm for (E).

suggests that a portion of NI01 should specialize in binding to the upper leaflet and be plastic enough to orchestrate protein re-assembly into pores. β Hairpins and bent α helices are common folding topologies that induce membrane thinning and exfoliation (Jang et al., 2006; Pyne et al., 2017). NI01 has three overlapping helical hairpins (Figure 1A). The two terminal hairpins have similar up-and-down topologies, in which individual helices are clearly separated by extended turns (Figure 1B). With the N- and C-terminal helices being twice the length of the central helices, the terminal hairpins have the capacity for transmembrane insertion. In contrast, the two central helices are arranged into an α-α corner via a kink at an obtuse angle, which constrains the helices into a more open hairpin conformation (Figures 1B and S6). A boomerang-like shape of this hairpin could make it lie flat on membrane surfaces, favoring membrane thinning over transmembrane poration (Figure S6).

Each Mode of the Mechanism Is Activated by a Specific Two-Helix Segment of NI01

To gain more insight into these predictions, all three hairpins—α1α2, α2α3, and α3α4 (Figure 1A), were synthesized (Figure S1), characterized (Figure S7), and imaged by AFM on SLBs (Figure 4). The first two hairpins showed strikingly distinctive behaviors, each supporting exclusively one mode of the mechanism observed for NI01 (Figure 4).

The first hairpin, α1α2, formed extended petal-like pores that ran parallel to each other without branching. The regions of thinned membranes that in NI01 served as branching points for the pores were absent in SLBs treated with α1α2. In contrast, membrane thinning was apparent in SLBs treated with α2α3, with no indication of transmembrane pores. Although the regions imaged for α2α3 were similar in size and morphology to those formed by NI01, the petal-like pores of α1α2 appeared thinner and more extended when compared with those of NI01 (Figure 4). Wide, circular pores were dominant in SLBs treated with α3α4, with membrane-thinning patches being also abundant, which together indicate that α3α4 induced a mixed mode of membrane disruption (Figure 4).
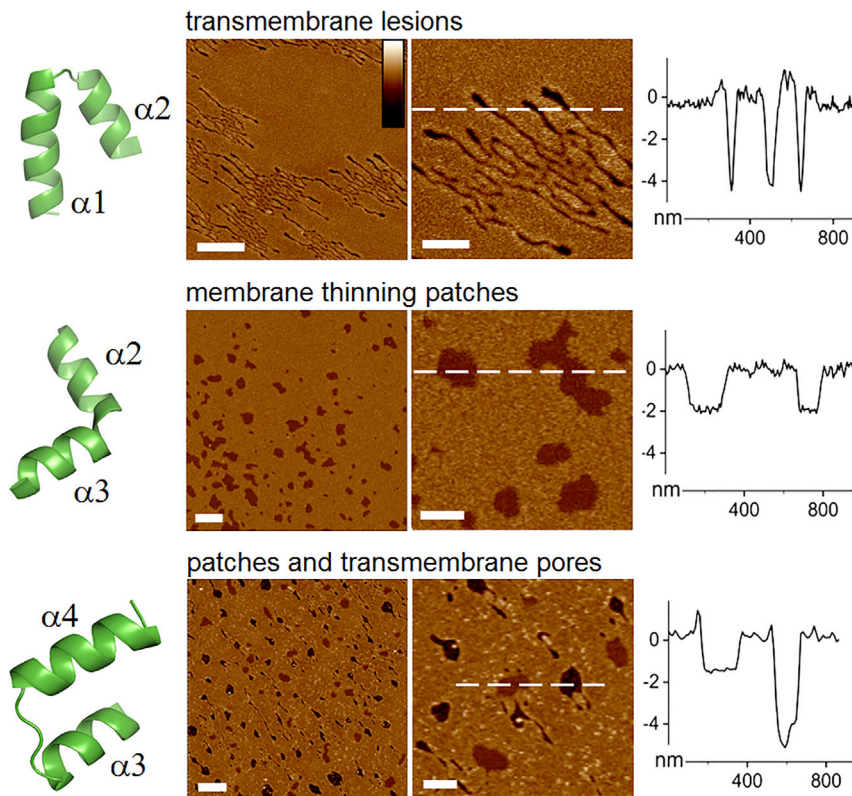
Figure 4. Membrane Poration Modes by Two-Helix Hairpins

In liquid AFM topography images of SLBs mimicking bacterial membranes treated with two-helix hairpins derived from NI01. The images were taken within the first 5 min of incubation with each hairpin (0.25 μM). Height profiles are measured along the highlighted lines. Color scale bar is 15 nm, length scale bars are 500 nm for the low magnification images (left) and 200 nm for the high magnification images (right). The two-helix hairpins are isolated segments of the reported crystal structure.

In these experiments, it is evident that membrane thinning patches occur only when α3 is present (Figure 4). Both α2α3 and α3α4 incorporate this helix and α3α4 is the only one of the three hairpins that induces the two membrane rupture modes. Thus, α3 appears to support the interplay of rupture modes favored by other helices. Further evidence for this was derived from the behavior of the two terminal three-helix hairpins, which were also produced as individual sequences (Figure S1). The N-terminal hairpin (α1α2α3) should combine two rupture modes: transmembrane lesions of α1α2 and thinned patches of α2α3, but without the synergy characteristic of NI01 manifesting in the conserved combined patterns of thinned patches and petals. For the C-terminal three-helix hairpin (α2α3α4) membrane thinning is expected to dominate as the synergy was already lacking in α3α4, and α2α3 did not form transmembrane pores. Consistent with this reasoning, the two predicted modes of membrane disruption were evident for α1α2α3 (Figure S8A). Although circular transmembrane pores could be detected for α2α3α4, these were much smaller in size, which contrasted with the abundance of thinned membrane regions caused by this hairpin (Figure S8A). The two three-helix hairpins were partially folded in solution, indicating impaired cooperativity of folding in solution when compared with that of NI01 (Figure S8B). Comparable helical content in solution was recorded for α3α4, which is notable given that α1α2 and α2α3 were unfolded (Figure S7). As for these two-helix hairpins, helicity sharply increased upon membrane binding for the terminal hairpins (Figures S7 and S8B) The results indicate that two- and three-helix hairpins containing α3 form membrane thinning patches, which emphasizes the mediatory role of this helix in supporting the interplay of the different modes of membrane disruption.

The C-terminal helix, α4, is the only helix in NI01 interacting with all other helices via the aromatic pairs. It is also a part of α3α4, which is the only two-helix hairpin that folds in solution (Figure 1). In α2α3α4, α2 and α3 share no single aromatic pair between them. H25 is an exception in that it is located in the central turn

connecting the two helices. The residue forms an aromatic pair with the terminal W50, which appears important for directing the insertion of α4. In addition, H25 is cationic, suggesting that it may bind to anionic lipids. Indeed, in both crystal forms H25 was observed to bind to SO_4^{2-} (Figure S9). In antimicrobial peptides similar electrostatic interactions are formed between phosphate groups and cationic residues, which in NI01 are represented by lysine (Figure 1A). Consistent with the exothermic phase in the ITC measurements (Figure 2C), the residue displaces water from the phosphate and strongly binds to it. The formed interactions are strong enough for membrane binding and cooperative enough to allow different disruption modes to manifest in synergy, one distinctive, conserved mechanism.

To test these conventions, all lysines were replaced with arginines in an all-arginine mutant of NI01, R-NI01 (Figure 1A). Unlike lysine, arginine is positively charged at all stages of membrane binding and insertion and traps more phosphate and water by providing five hydrogen-bond donors (Li et al., 2013). This difference manifests in a tighter binding to membrane surfaces, and, as shown elsewhere, limits protein insertion into the upper leaflet of the bilayer (Pyne et al., 2017). Replacing H25 with arginine preserves the positive charge in the site, but it also eliminates the H25-W50 pair compromising cooperativity in interactions between helices and the ability of α4 to insert. Indeed, this mutant produced exclusively thinning patches in the membranes, which were strikingly similar to those observed for α2α3 (Figures 4 and S10A). Furthermore, R-NI01 was 50% less helical than NI01 (Figure S10B). The loss in helicity was restored upon binding to phospholipid membranes (Figure S10B). This behavior was similar to that of the three-helix hairpins, which were considerably less helical in solution than NI01, but whose helical content increased in membranes (Figure S8B). These results indicate that this mutation had a detrimental effect on NI01 folding in solution and its multi-mode mechanism in membranes.

The importance of these findings is 2-fold. First, the analysis of disruption mechanisms by individual hairpins confirm that NI01 exhibits a conserved, synergistic mechanism of membrane disruption. This is ensured by the cooperative folding of NI01 and tertiary contacts of its constituent helices. Each of these helices makes an important contribution to the complex pattern of this mechanism, but none of them is sufficient individually. Second, all hairpin derivatives disrupt bacterial mimetic membranes. This suggests that all of the hairpins are antimicrobial and that their antimicrobial activities do not require a specific receptor to target bacteria, and therefore the antimicrobial activity of NI01 is not stereoselective.

Synergy in the Multi-Mode Mechanism Determines the Biological Selectivity of the Protein

Considering the first point, NI01 and all of its derivatives exhibited comparable levels of antibacterial activity. Minimum inhibitory concentrations (MICs) were similar to those obtained for conventional antibiotics (Table S2). Noteworthy differences were observed in MICs for Gram-positive *S. aureus* and Gram-negative *P. aeruginosa*. NI01, α1α2, and α3α4 were equally effective against *S. aureus* and ineffective against *P. aeruginosa*. Intriguingly, α2α3 showed a reversed trend, which may be attributed to differences in the cell-wall structure of the bacteria. The peptidoglycan layer of Gram-positive cells is rich in anionic teichoic polymers, which might prevent α2α3 from reaching the cytoplasmic membrane (Yeaman and Yount, 2003). This proposition is supported by the observation that α2α3 remained largely unfolded in membranes and hence is subject to conformational fluctuations caused by binding to the teichoic polymers (Figure S7). All other hairpins and R-NI01 responded to membrane binding with sharp increases in helicity. Other Gram-positive bacteria, *B. subtilis* and *M. luteus*, proved to be susceptible to all of the NI01 derivatives used (Table S2). Peptidoglycans in these bacteria undergo continuous transformations from thick to thin layers, which makes their membranes more vulnerable to the attack by α2α3 (Tocheva et al., 2013; Vollmer, 2008). Consistent with the lack of activity against *S. aureus*, α2α3 failed to affect methicillin-resistant *S. aureus* (MRSA) strains. NI01 and the other two-helix hairpins maintained similar levels of activity against these pathogens when compared with those for the susceptible strain (Tables S2 and S3). The three-helix hairpins were less active against MRSA. Both these hairpins incorporate α2α3 that was inactive against any of the *S. aureus* strains tested. Therefore, the impact of thicker peptidoglycan layers of MRSA (García et al., 2017) on their activity is expected to be greater (Tables S2 and S3). Another notable trend was observed for Gram-negative bacteria. NI01 and its derivatives appeared to be active only against *E. coli*. Similar to peptidoglycan layers in Gram-positive bacteria, lipopolysaccharide (LPS) layers represent a key virulence factor for Gram-negative membranes. To probe this, two additional *E. coli* strains were tested: a short-chain LPS or rough strain, SBS363, and a smooth strain comprising full-length, mature O-chains, ML35 (Ebbensgaard et al., 2018). All derivatives were active against the rough, more susceptible type, but the smooth type was resistant to all two-helix hairpins, except α1α2 (Table S3).

Considering the second point, NI01 was re-made into an all-D form (Figure S1). The protein adopted helical conformations that quantitatively mirrored those of the wild-type all-L NI01 in both solution and membranes (Figures 2A and S4A). In bacterial membranes the all-D form revealed a strikingly similar pattern to that of the all-L form (Figure S11), and both epimeric forms exhibited comparable antibacterial activities across all bacteria and strains tested (Tables S2 and S3). Taken together the results of these biological tests confirmed the antibacterial properties of NI01, with stronger activities observed for the derivatives exhibiting transmembrane disruption modes.

Bacteriocins, unlike host defense peptides or helminth defense molecules (Hammond et al., 2019), do not originate from multicellular organisms. However, there can be a selective pressure on bacteria residing in human hosts to remain in a commensal state. Consequently, bacteriocins produced by these bacteria should be able to differentiate between bacterial and host cells. For therapeutic applications, this requirement extends to red blood cells, which are weakly anionic and can also be targeted by bacteriocins. In this regard, NI01 proved to be non-hemolytic in both L- and D-forms at concentrations equivalent to >100 x MICs against Gram-positive strains. This result was striking as all other derivatives caused appreciable hemolysis, except α2α3, which showed no hemolytic activity even at high concentrations (>600 μg/mL). These findings suggest that this hairpin re-balances antibacterial and hemolytic activities of NI01 by effectively diminishing the impact of the terminal helices, which favor transmembrane poration. Hemolytic activities drastically increased for R-NI01 and other hairpins, all of which lack the synergy of inter-helix interactions characteristic for NI01. As a consequence, these derivatives were incapable to differentiate between bacterial and erythrocytic membranes.

### Mechanistic Similarities with Other Four-Helix Bacteriocins

To this end, we have shown that NI01 exhibits a unique multi-mode mechanism of membrane disruption. To the best of our knowledge, this is also the first direct observation of bacteriocin-induced poration, which prompts an obvious comparison with other bacteriocins.

With this in mind, we performed a similar analysis for aureocin A53 (Figure 5A). This bacteriocin belongs to the same four-helix bundle group and its structure was recently solved by NMR spectroscopy (Figure 5B) (Acedo et al., 2016). As gauged by CD spectroscopy, the protein folded remarkably similar to that of NI01, with the two proteins having a nearly identical helical content (Figure 5C). A53 was as stable as NI01 with (T_M) of ~54°C (Figure S12A), folded reversibly and independently of concentration (Figures S12B and S12C), and showed no changes at increasing TFE concentrations (Figure S12D). BLAST searches indicated a significant level of sequence homology between the two proteins (38% identity). The location and extent of turn regions and individual helices were also very similar, while hydrophobic, polar, and aromatic residues were well conserved (Figure 5A). Outside of the identity regions the exact sequence compositions of NI01 and A53 are different. Despite that the observed structural similarities suggest that A53 might exhibit a similar mechanism of membrane disruption.

AFM analyses of A53-treated anionic membranes showed disruption modes similar to those recorded for NI01: membrane thinning patches and transmembrane lesions and pores (Figure 5D). The patches were more extended than those for NI01. The petal-like lesions were morphologically similar to those of NI01, also ending with circular pores and grew out of the patches. Depth profiles for each mode were identical for the two bacteriocins (Figures 3C and 5E). Overall, the same characteristics of membrane disruption were evident for both proteins, which exhibited the same folding topology, sequence length, and helical content. The variations in the mechanisms may be attributed to amino acid permutations in helical and turn regions of the two proteins.

DISCUSSION

Bacteriocins have long been recognized as highly specific antibiotics that bacteria develop to outcompete closely related strains. It has also been long thought that these small proteins act by porating bacterial membranes like other pore-forming toxins, some antibiotics, and host-defense peptides (Hechard and Sahl, 2002) However, direct evidence for bacteriocin-promoted poration has been lacking, despite the fact that bacteriocins belong to a distinctive family of host defense molecules with a common protein fold (Cotter et al., 2013; Acedo et al., 2018; Hechard and Sahl, 2002). Although several bacteriocin structures have been solved (Lohans et al., 2013; González et al., 2000; Acedo et al., 2016), the way their structural features specify antimicrobial mechanisms remains obscure. This study partially filled this gap by
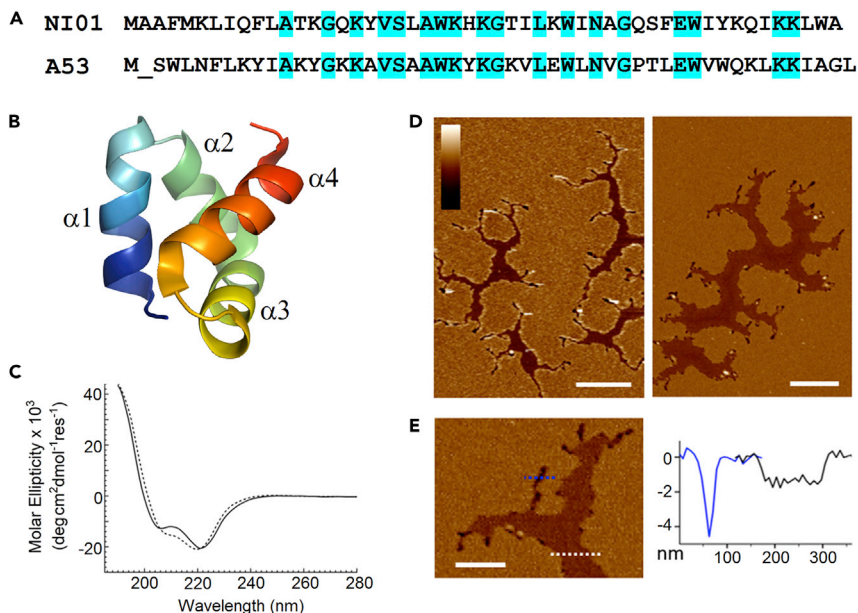
Figure 5. Comparative Behavior of Aureocin A53

(A) Amino acid sequences of NI01 and A53. Identical amino acids are highlighted in cyan.

(B) NMR solution structure of A53 bacteriocin (PDB entry 2N8O rendered by PyMol) (Acedo et al., 2016).

(C) CD spectra for NI01 (dashed line) and A53 (black line) (20 μM protein) in 10 mM phosphate buffer.

(D) Topography AFM images of anionic SLBs treated with A53 (0.25 μM).

(E) A higher magnification image with height profiles measured along the highlighted lines. Color and length scale bars are 15 and 500 nm (D) and 200 nm (E), respectively.

solving the fold of an archetypal bacteriocin, epidermicin NI01, and correlating it with a unique mechanism comprising several distinctive modes of membrane disruption, in contrast to alternative scenarios that assume one poration mode per membrane-disrupting agent. Furthermore, we experimentally demonstrated that it is the cooperativity of interactions between the structural constituents, helical hairpins, which orchestrates multiple modes into one synergistic process. For example, the central hairpin, α2α3, was found to have a direct and reciprocal impact on the terminal helices translating different disruption modes into one dynamic process. This mechanism is conserved, favors anionic membranes, and is not stereoselective. Thinning patches and transmembrane petals tended to expand with time, whereas their morphology and depths did not change. This type of propagation is likely to occur at the expense of NI01 monomers oligomerizing on and in the lipid bilayers. Similarly, the transition from a patch to a lesion is likely to involve an oligomerization event. Existing models of membrane disruption by pore-forming proteins suggest that these proteins associate via their hydrophobic surfaces that become exposed as their cationic surfaces face anionic lipids (González et al., 2000; Michalek et al., 2013; Acedo et al., 2016). The models appear universal for proteins adopting four- and five-helix folds: acanthaporin produced by pathogenic amebae, natural killer cell lysins, and bacteriocins analogous to NI01 and A53 may have different biological functions, but all share similar characteristics of high stability, surface charge, and conserved folding and hence may disrupt membranes via similar mechanisms. It remains unclear, however, if membrane disruption involves a minimal, active oligomer that defines the size and dynamics of the forming pores, as was shown for single-helix antimicrobial peptides (Pyne et al., 2017).

To sum up, our results revealed that the four-helix bundle organization of bacteriocins is necessary to complete such a highly regulated and sophisticated mechanism. The fold itself encodes this decisively physical means of selective membrane attack that is likely to hold true for other single-chain bacteriocins. The behavior of another four-helix bacteriocin, A53, supports this conclusion.

Limitations of the Study

The exact reason for this complex mechanism is unclear. One possibility is that four-helix folds may better adapt to overcome a wide range of resistant membranes. The subtlety with which constituent helices

cooperate is what makes bacteriocins less susceptible to acquired antibacterial resistance. This contrasts with host-defense peptides and membrane-active antibiotics that rely on a single disruption mode and are less fit against emerging strategies of membrane resistance (Needham and Trent, 2013). Another question is whether a multi-mode membrane disruption constitutes a common hallmark of bacteriocins, which may distinguish these proteins from other pore-forming and antibacterial molecules. Extensive site-directed mutagenesis of bacteriocin sequences together with AFM analysis of their action on bacterial membranes may provide additional insights into the mechanism. These proposals merit further independent investigations.

Resource Availability

Lead Contact

Further information and requests for resources and reagents should be directed to and will be fulfilled by the Lead Contact, Maxim G Ryadnov (max.ryadnov@npl.co.uk).

Materials Availability

This study did not generate new unique reagents.

Data and Code Availability

The data supporting the findings of this study is available within this paper and its Supplemental Information. Coordinates and structure factors generated during this study are deposited in PDB. The accession numbers for the structure of NI01 in two crystal forms ($P2_12_12$, $C222$) reported in this paper are PDB: 6SIF, 6SIG.

METHODS

All methods can be found in the accompanying Transparent Methods supplemental file.

SUPPLEMENTAL INFORMATION

Supplemental Information can be found online at https://doi.org/10.1016/j.isci.2020.101423.

AUTHOR CONTRIBUTIONS

All authors designed the experiments and analyzed and interpreted the data. K.H., H.L., S.H., F.D., B.N., and J.R. performed the research. B.W.H., M.U., J.P.D., and M.G.R. supervised the research. M.G.R wrote the manuscript. All authors contributed to the editing of the manuscript.

DECLARATION OF INTERESTS

A patent application has been filed on the subject matter of the manuscript.

REFERENCES

Acedo, J.Z., Chiorean, S., Vederas, J.C., and van Belkum, M.J. (2018). The expanding structural variety among bacteriocins from Gram-positive bacteria. FEMS Microbiol. Rev. *42*, 805–828.

Acedo, J.Z., van Belkum, M.J., Lohans, C.T., Towle, K.M., Miskolzie, M., and Vederas, J.C. (2016). Nuclear magnetic resonance solution

structures of lacticin Q and aureocin A53 reveal a structural motif conserved among leaderless bacteriocins with broad-spectrum activity. Biochemistry *55*, 733–742.

Arnison, P.G., Bibb, M.J., Bierbaum, G., Bowers, A.A., Bugni, T.S., Bulaj, G., Camarero, J.A., Campopiano, D.J., Challis, G.L., Clardy, J., et al.

(2013). Ribosomally synthesized and post-translationally modified peptide natural products: overview and recommendations for a universal nomenclature. Nat. Prod. Rep. *30*, 108–160.

Cotter, P.D., Hill, C., and Ross, R.P. (2005). Bacteriocins: developing innate immunity for food. Nat. Rev. Microbiol. *3*, 777–788.

Cotter, P.D., Ross, R.P., and Hill, C. (2013). Bacteriocins – a viable alternative to antibiotics? Nat. Rev. Microbiol. *11*, 95–105.

Ebbensgaard, A., Mordhorst, H., Aarestrup, F.M., and Hansen, E.B. (2018). The role of outer membrane proteins and lipopolysaccharides for the sensitivity of *Escherichia coli* to antimicrobial peptides. Front. Microbiol. *9*, 2153.

García, A.B., Viñuela-Prieto, J.M., López-González, L., and Candel, F.J. (2017). Correlation between resistance mechanisms in *Staphylococcus aureus* and cell wall and septum thickening. Infect. Drug Resist. *10*, 353–356.

González, C., Langdon, G.M., Bruix, M., Gálvez, A., Valdivia, E., Maqueda, M., and Rico, M. (2000). Bacteriocin AS-48, a microbial cyclic polypeptide structurally and functionally related to mammalian NK-lysin. Proc. Natl. Acad. Sci. U S A *97*, 11221–11226.

Hammond, K., Lewis, H., Faruqui, N., Russell, C., Hoogenboom, B.W., and Ryadnov, M.G. (2019). Helminth defense molecules as design templates for membrane active antibiotics. ACS Infect. Dis. *5*, 1471–1479.

Heath, G.R., Harrison, P.L., Strong, P.N., Evans, S.D., and Miller, K. (2018). Visualization of diffusion limited antimicrobial peptide attack on supported lipid membranes. Soft Matter. *14*, 6146–6154.

Hechard, Y., and Sahl, H.G. (2002). Mode of action of modified and unmodified bacteriocins from Gram positive bacteria. Biochimie *84*, 545–557.

Iacovach, I., Bischofberger, M., and van der Goot, F.G. (2010). Structure and assembly of pore-forming proteins. Curr. Opin. Struct. Biol. *20*, 241–246.

Jang, H., Ma, B., Woolf, T.B., and Nussinov, R. (2006). Interaction of protegrin-1 with lipid bilayers: membrane thinning effect. Biophys. J. *91*, 2848–2859.

Kelly, S.M., Jess, T.J., and Price, N.C. (2005). How to study proteins by circular dichroism. Biochim. Biophys. Acta *1751*, 119–139.

Khatib, T.O., Stevenson, H., Yeaman, M.R., Bayer, A.S., and Pokorny, A. (2016). Binding of daptomycin to anionic lipid vesicles is reduced in the presence of lysyl-phosphatidylglycerol. Antimicrob. Agents Chemother. *60*, 5051–5053.

Koehbach, J., and Craik, D.J. (2019). The vast structural diversity of antimicrobial peptides. Trends Pharmacol. Sci. *40*, 517–528.

Krissinel, E., and Henrick, K. (2007). Inference of macromolecular assemblies from crystalline state. J. Mol. Biol. *372*, 774–797.

Lazar, V., Martins, A., Spohn, R., Daruka, L., Grézal, G., Fekete, G., Számel, M., Jangir, P.K., Kintses, B., Csörgő, B., et al. (2018). Antibiotic-resistant bacteria show widespread collateral sensitivity to antimicrobial peptides. Nat. Microbiol. *3*, 718–731.

Li, L., Vorobyov, I., and Allen, T.W. (2013). The different interactions of lysine and arginine side chains with lipid membranes. J. Phys. Chem. B *117*, 11906–11920.

Lin, W.-C., Blanchette, C.D., Ratto, T.V., and Longo, M.L. (2006). Lipid asymmetry in DLPC/DSPC-supported lipid bilayers: a combined AFM and fluorescence microscopy study. Biophys. J. *90*, 228–237.

Lohans, C.T., Towle, K.M., Miskolzie, M., McKay, R.T., van Belkum, M.J., McMullen, L.M., and Vederas, J.C. (2013). Solution structures of the linear leaderless bacteriocins enterocin 7A and 7B resemble carnocyclin A, a circular antimicrobial peptide. Biochemistry *52*, 3987–3994.

Mecke, A., Lee, D.K., Ramamoorthy, A., Orr, B.G., and Banaszak Holl, M.M. (2005). Membrane thinning due to antimicrobial peptide binding: an atomic force microscopy study of MSI-78 in lipid bilayers. Biophys. J. *89*, 4043–4050.

Michalek, M., Sönnichsen, F.D., Wechselberger, R., Dingley, A.J., Hung, C.W., Kopp, A., Wienk, H., Simanski, M., Herbst, R., Lorenzen, I., et al. (2013). Structure and function of a unique pore-forming protein from a pathogenic acanthamoeba. Nat. Chem. Biol. *9*, 37–42.

Mingeot-Leclercq, M.-P., Deleu, M., Brasseur, R., and Dufrêne, Y.F. (2008). Atomic force microscopy of supported lipid bilayers. Nat. Protoc. *3*, 1654–1659.

Needham, B.D., and Trent, M.S. (2013). Fortifying the barrier: the impact of lipid A remodeling on bacterial pathogenesis. Nat. Rev. Microbiol. *11*, 467–481.

Parker, M.W., and Feil, S.C. (2005). Pore-forming protein toxins: from structure to function. Prog. Biophys. Mol. Biol. *88*, 91–142.

Pfeil, M.P., Pyne, A.L.B., Losasso, V., Ravi, J., Lamarre, B., Faruqui, N., Alkassem, H., Hammond, K., Judge, P.J., Winn, M., et al. (2018). Tuneable poration: host defense peptides as sequence probes for antimicrobial mechanisms. Sci. Rep. *8*, 14926.

Pyne, A., Pfeil, M.P., Bennett, I., Ravi, J., Iavicoli, P., Lamarre, B., Roethke, A., Ray, S., Jiang, H., Bella, A., et al. (2017). Engineering monolayer poration for rapid exfoliation of microbial membranes. Chem. Sci. *8*, 1105–1115.

Rakowska, P.D., Jiang, H., Ray, S., Pyne, A., Lamarre, B., Carr, M., Judge, P.J., Ravi, J., Gerling, U.I., Koksch, B., et al. (2013). Nanoscale imaging reveals laterally expanding antimicrobial pores in lipid bilayers. Proc. Natl. Acad. Sci. U S A *110*, 8918–8923.

Roccatano, D., Colombo, G., Fioroni, M., and Mark, A.E. (2002). Mechanism by which 2,2,2-trifluoroethanol/water mixtures stabilize secondary-structure formation in peptides: a molecular dynamics study. Proc. Natl. Acad. Sci. U S A *99*, 12179–12184.

Sandiford, S., and Upton, M. (2012). Identification, characterization, and recombinant expression of epidermicin NI01, a novel unmodified bacteriocin produced by *Staphylococcus epidermidis* that displays potent activity against Staphylococci. Antimicrob. Agents Chemother. *56*, 1539–1547.

Seelig, J. (2004). Thermodynamics of lipid-peptide interactions. Biochim. Biophys. Acta *1666*, 40–50.

Tocheva, E.I., López-Garrido, J., Hughes, H.V., Fredlund, J., Kuru, E., Vannieuwenhze, M.S., Brun, Y.V., Pogliano, K., and Jensen, G.J. (2013). Peptidoglycan transformations during *Bacillus subtilis* sporulation. Mol. Microbiol. *88*, 673–686.

Vollmer, W. (2008). Structural variation in the glycan strands of bacterial peptidoglycan. FEMS Microbiol. Rev. *32*, 287–306.

Yeaman, M.R., and Yount, N.Y. (2003). Mechanisms of antimicrobial peptide action and resistance. Pharmacol. Rev. *55*, 27–55.

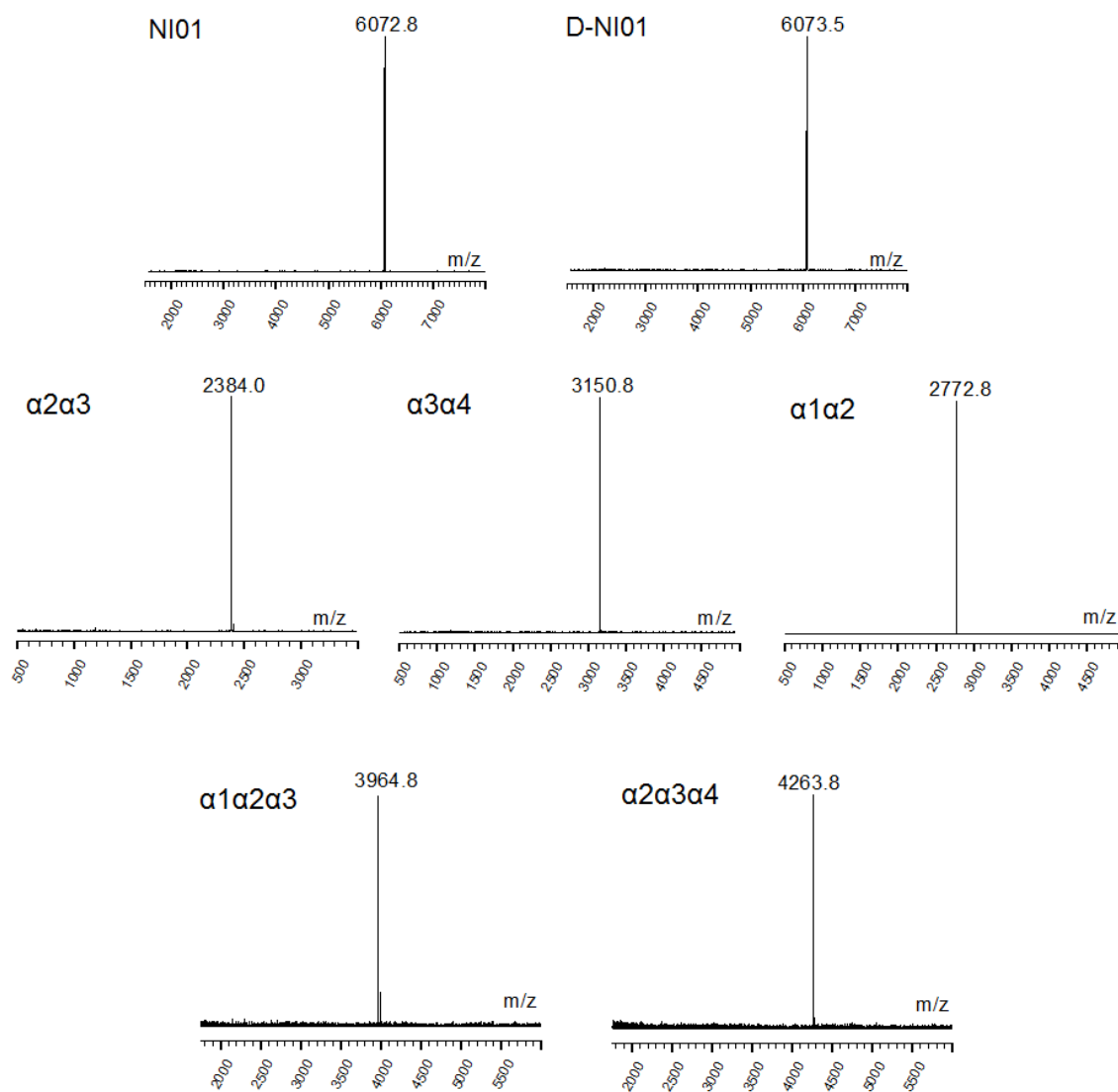# Supplemental Information

Flowering Poration—A Synergistic Multi-Mode

Antibacterial Mechanism by a Bacteriocin Fold

Katharine Hammond, Helen Lewis, Samantha Halliwell, Florie Desriac, Brunello Nardone, Jascindra Ravi, Bart W. Hoogenboom, Mathew Upton, Jeremy P. Derrick, and Maxim G. Ryadnov

Figure S1. Post-synthetic characterisation. Related to Figure 1. MALDI-ToF mass spectrometry spectra for purified NI01 and NI01 derivatives used in the study.
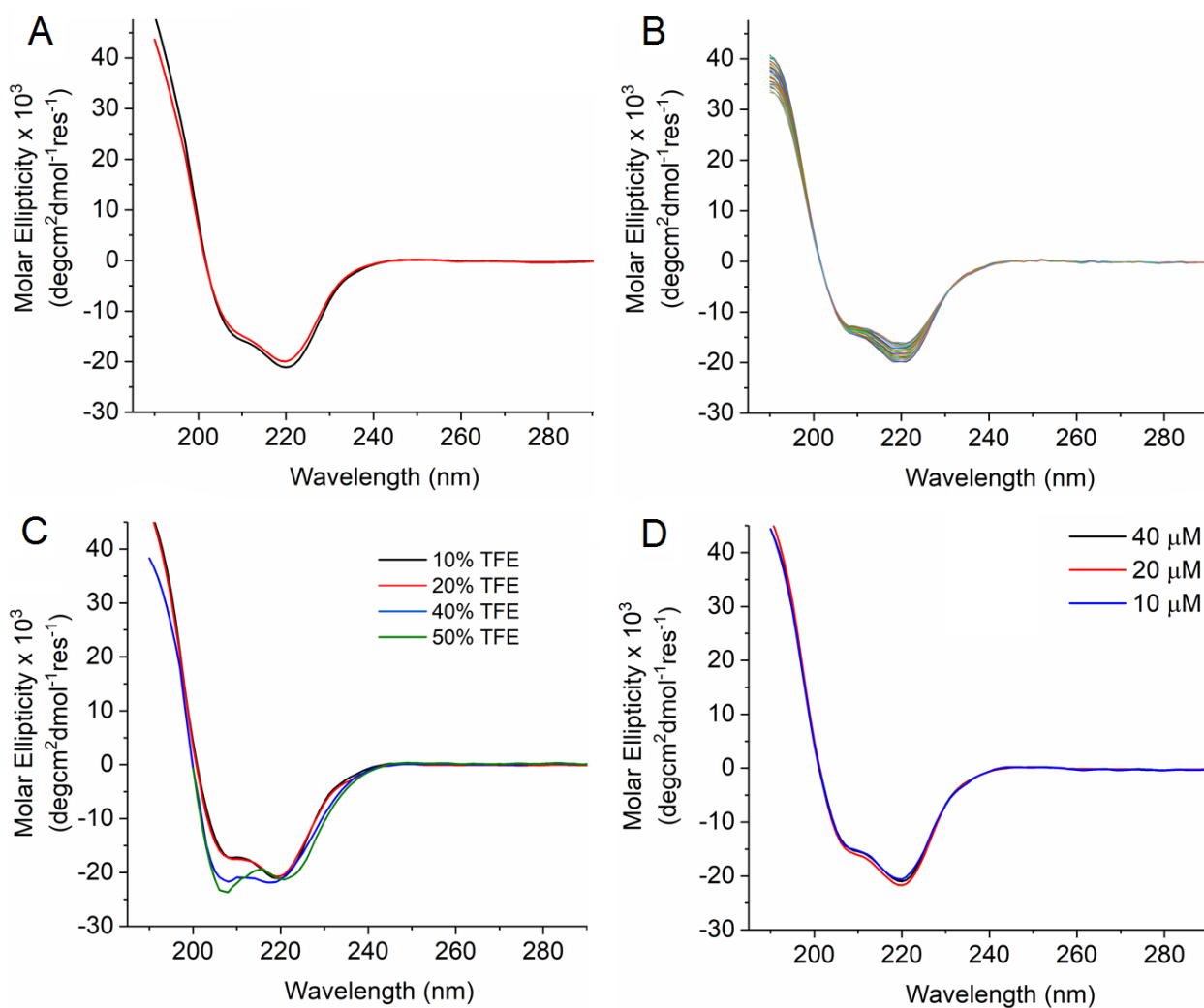
Figure S2. NI01 folding monitored by CD spectroscopy. Related to Figure 2. CD spectra for (A) NI01 recorded before (black line) and after (red line) thermal denaturation; (B) NI01 recorded at 2 ℃ intervals during the thermal unfolding from 20 ℃ to 90 ℃; (C) NI01 at varied TFE concentrations; (D) NI01 at different protein concentrations. Folding conditions: 20 µM protein, pH 7.4, 10 mM phosphate buffer, 20˚C.
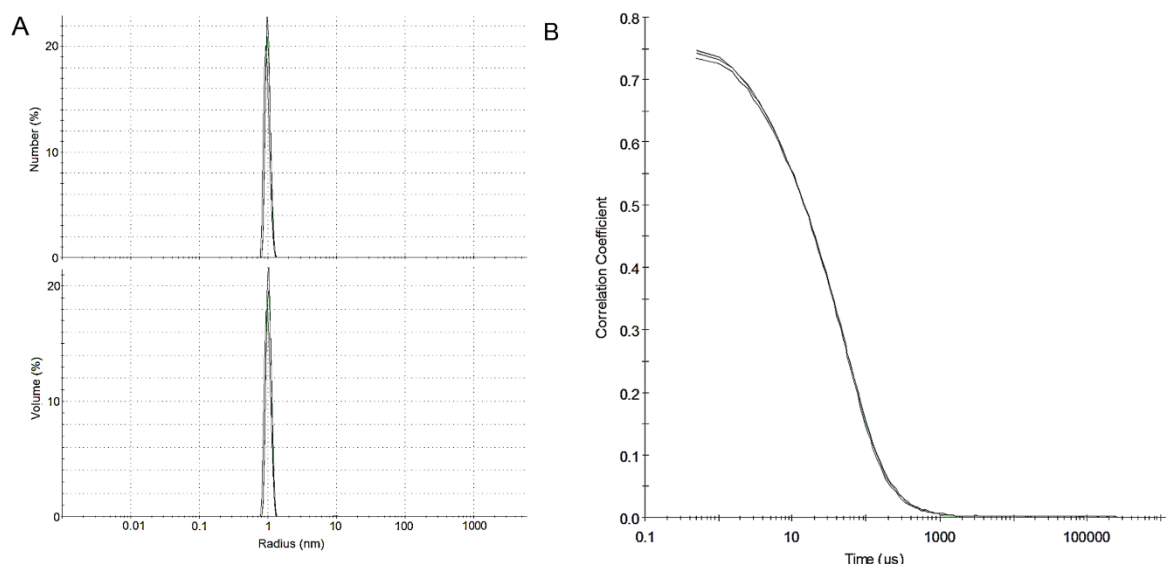
Figure S3. NI01 monodispersity in solution. Related to Figure 1 and Figure 2. (A) Size distributions by dynamic light scattering by number and volume for NI01 (0.9 mM) in 10 mM phosphate buffer, pH 7.4. (B) Correlograms showing rapid correlation decreases from high intercepts, which is characteristic of monodisperse, small particles.
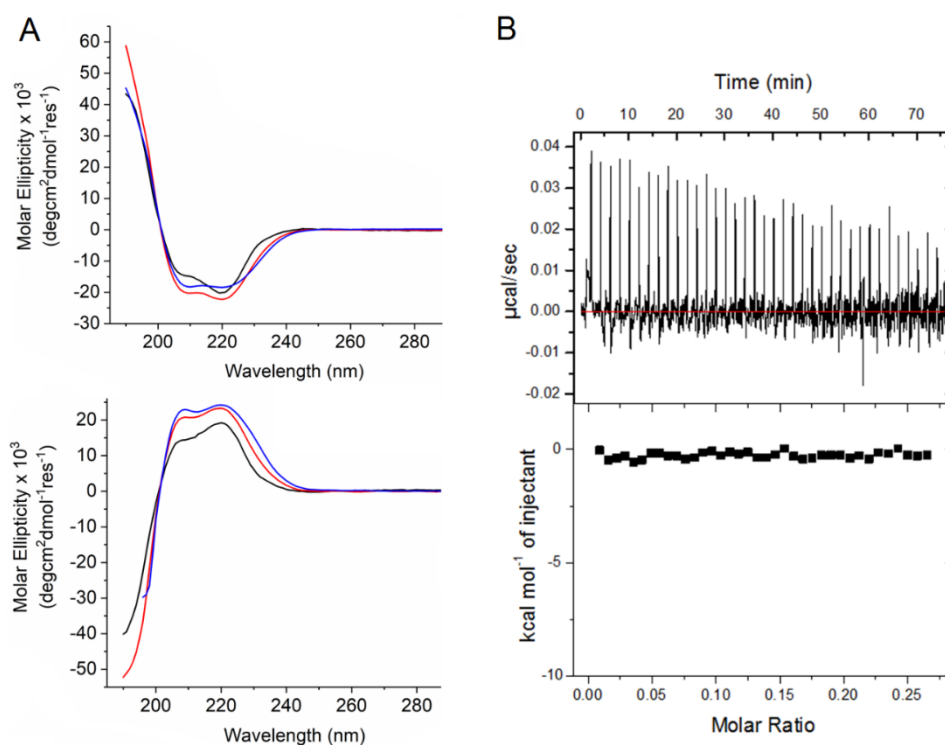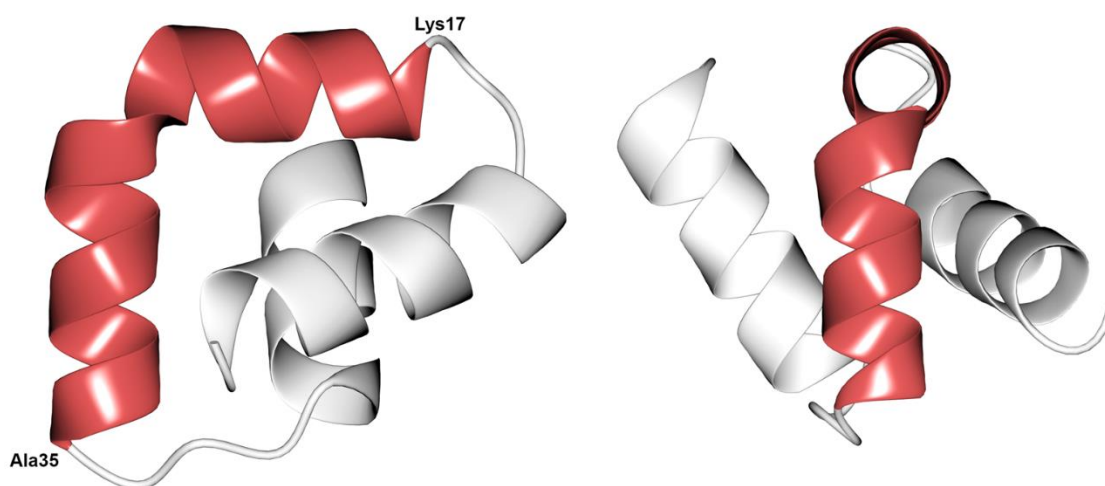

Figure S4. NI01 interactions with reconstituted phospholipid membranes. Related to Figure 2. (A) CD spectra for NI01 (upper) and its all-D form (lower) (20 µM) in phosphate buffer (black line) and in anionic (blue line) and zwitterionic (red line) membranes at 100 lipid/protein (L/P) ratios. (B) Isothermal titration calorimetry of NI01 (0.5 mM) binding to mammalian mimetic membranes. Heat absorbed (μcal/s) for each isotherm is plotted versus titration time (upper panel). Integrated heats (kcal/mol) are plotted versus protein-lipid molar ratios (lower panel).
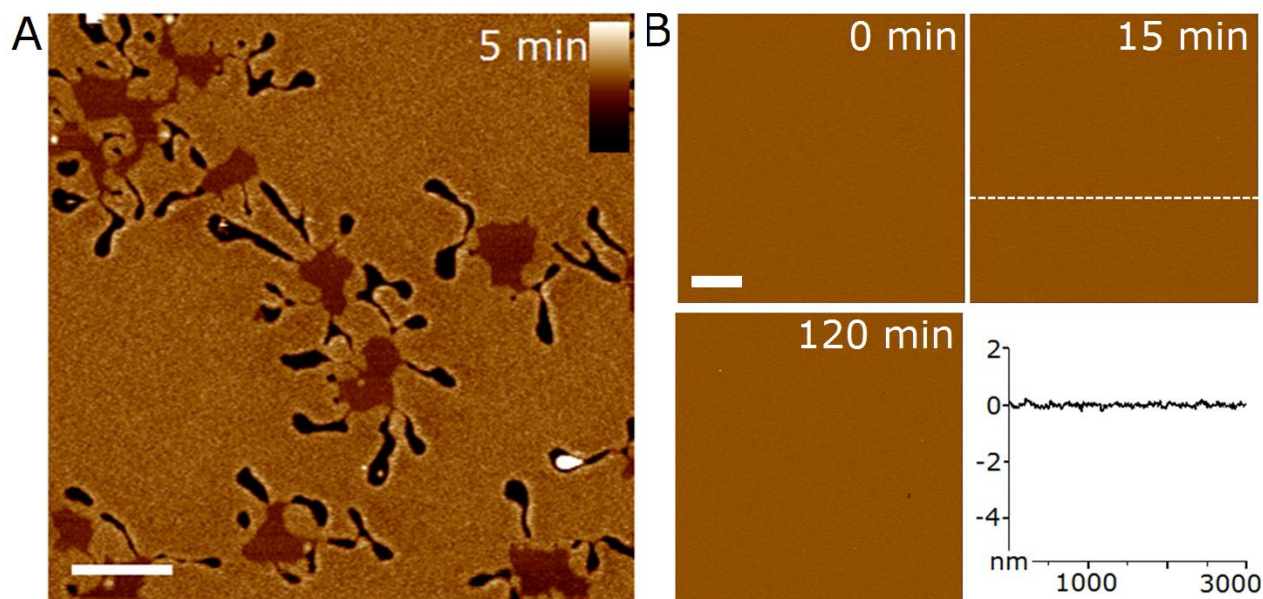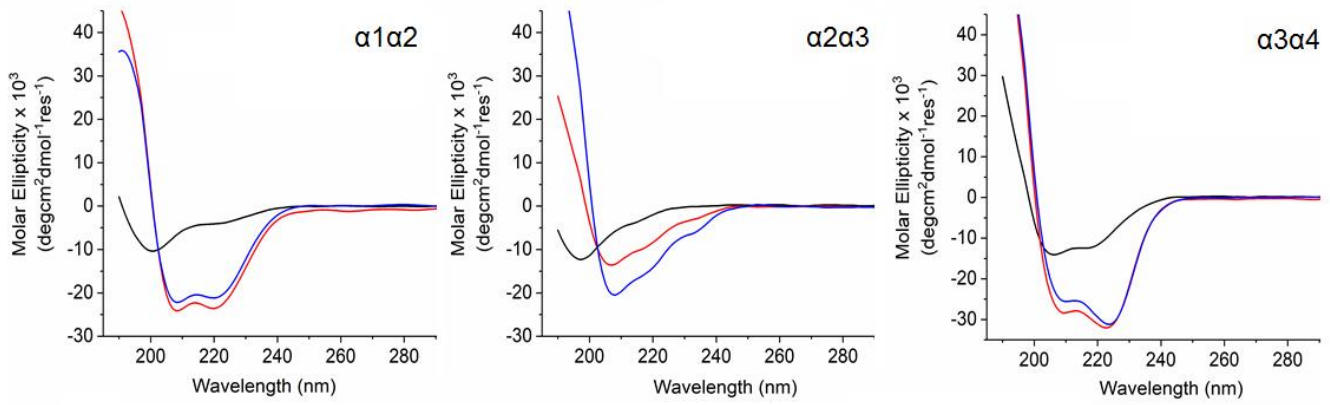
Figure S5. In-liquid AFM imaging of reconstituted phospholipid membranes incubated with NI01. **Related to Figure 3.** (A) Topography of SLBs mimicking bacterial membranes treated with NI01 (0.25 µM). (B) Topography micrographs of SLBs mimicking mammalian membranes treated with NI01 at higher concentrations (0.6 µM), with height profile as measured along the white, dashed line. Colour and length scale bars are 15 nm and 500 nm, respectively.

**Figure S6. A boomerang-like shape of the central hairpin, α2α3. Related to Figure 1.** Two different points of view are given to show that α2 and α3 are linked at an obtuse angle (left) forming a flat conformation (right).

Figure S7. Interactions of two-helix hairpins with reconstituted phospholipid membranes. **Related to Figure 1 and Figure 4.** CD spectra for the hairpins (20 µM) in phosphate buffer (black line) and in anionic (blue line) and zwitterionic (red line) membranes at 100 lipid/protein (L/P) ratios.
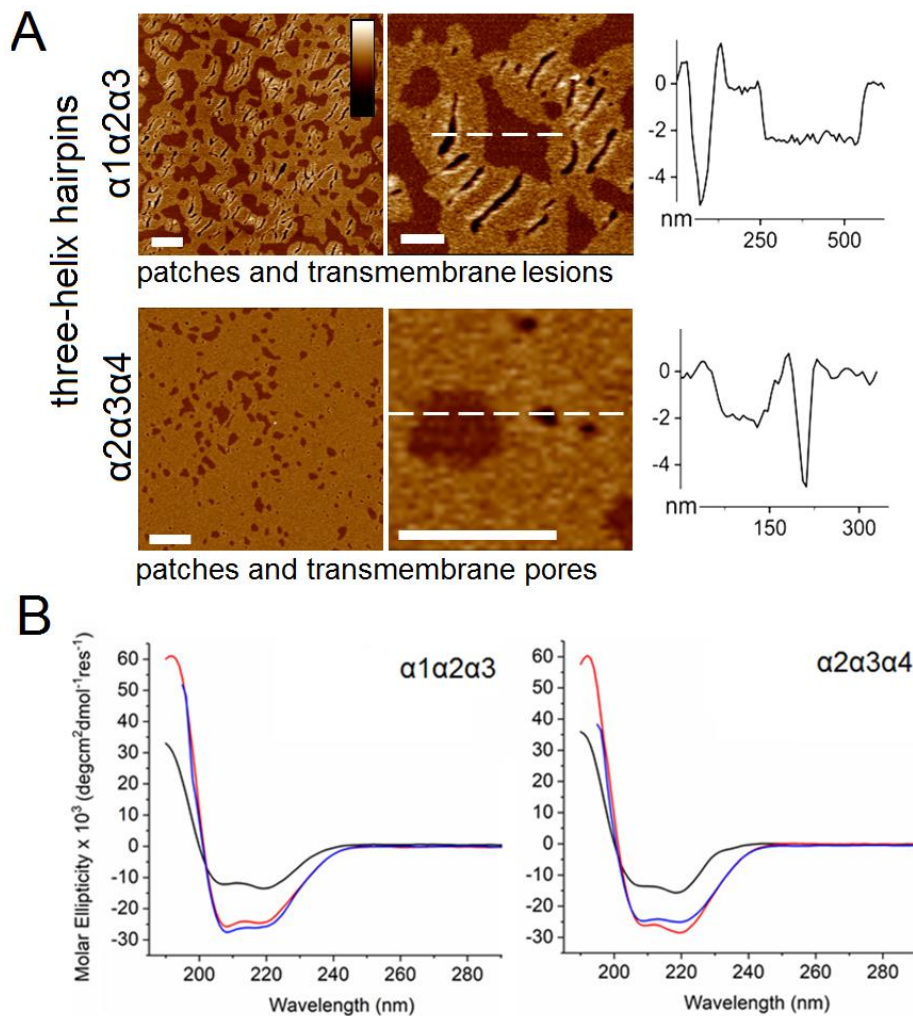
Figure S8. Three-helix hairpins. Related to Figure 1. (A) In-liquid AFM imaging of SLBs mimicking bacterial membranes incubated with the hairpins (0.25 µM). The images were taken within the first 5 min of incubation. Height profiles measured along the highlighted lines. Colour scale bar is 15 nm. Length scale bars are 500 nm (left) and 200 nm (right). (B) CD spectra for the hairpins (20 µM) in phosphate buffer (black line) and in anionic (blue line) and zwitterionic (red line) membranes at 100 lipid/protein (L/P) ratios.
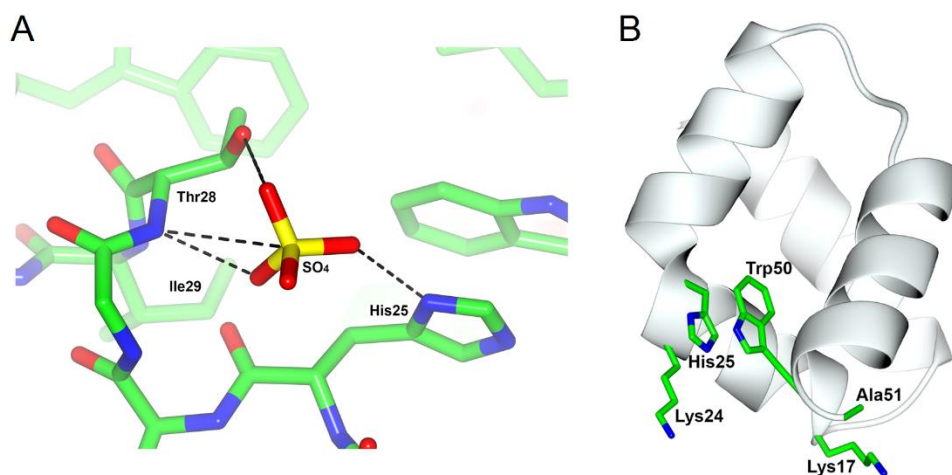
Figure S9. Cooperative structural arrangements of H25. **Related to Figure 1.** (A) A polar cluster at H25 in the central kink hosting a binding site for SO_4^{2-}. (B) Cooperative positioning of the residue forming an aromatic π-π pair with W50.
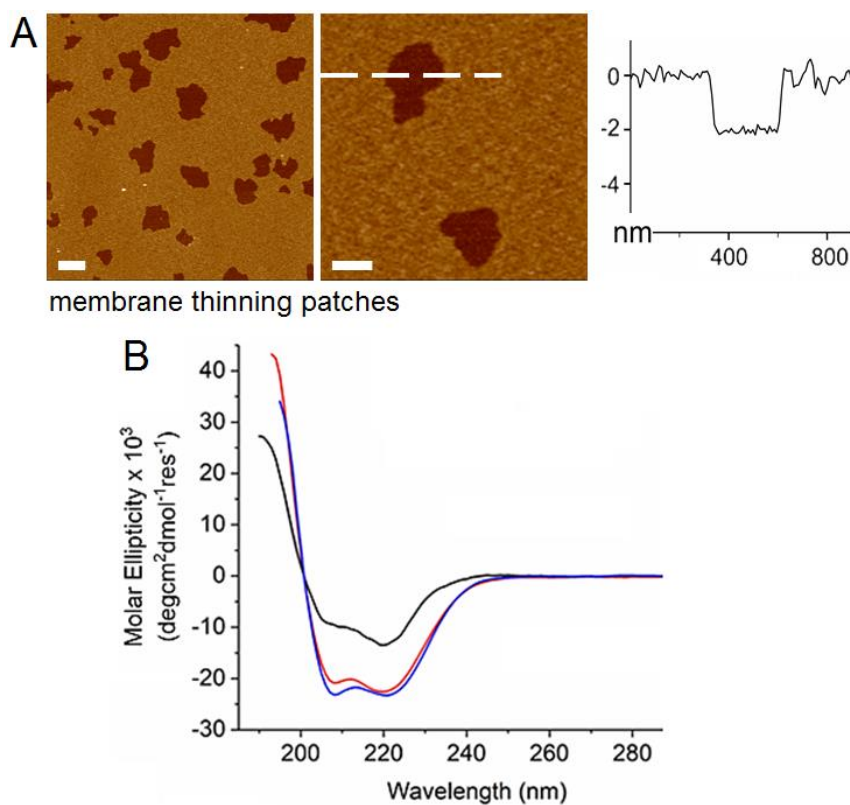
Figure S10. Arginine NI01 mutant, R-NI01. Related to Figure 1 and Figure 3. (A) In-liquid AFM imaging of SLBs mimicking bacterial membranes incubated with the mutant (0.25 μM). The images were taken within the first 5 min of incubation. Height profiles measured along the highlighted lines. Colour scale bar is 15 nm. Length scale bars are 500 nm (left) and 200 nm (right). (B) CD spectra for the mutant (20 μM) in phosphate buffer (black line) and in anionic (blue line) and zwitterionic (red line) membranes at 100 lipid/protein (L/P) ratios.
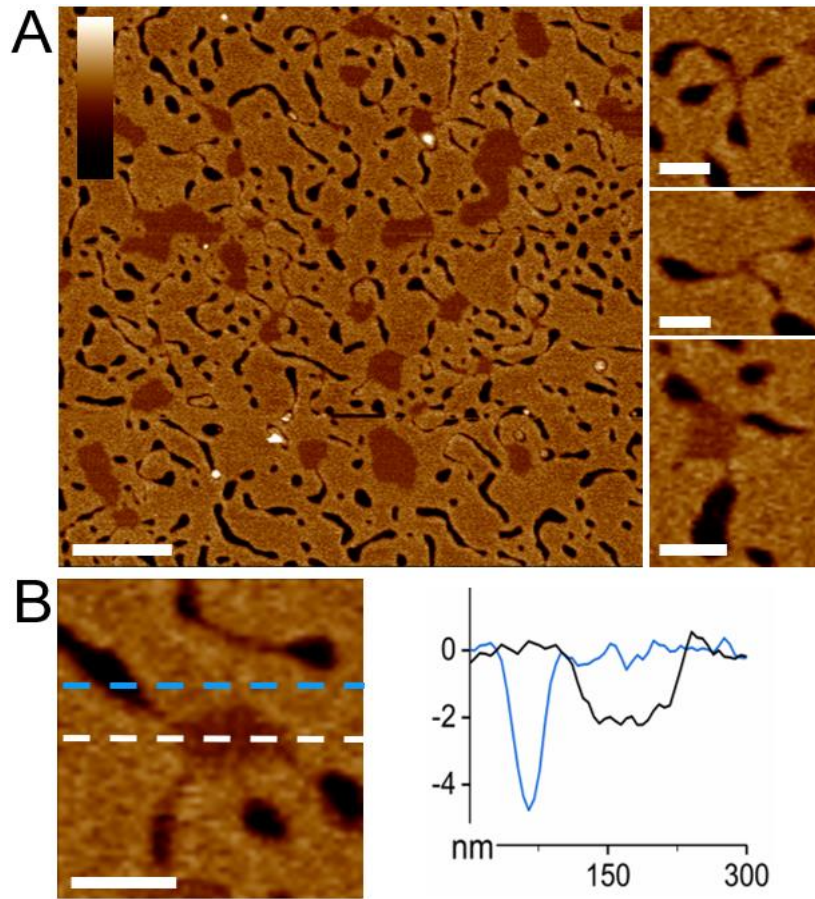
Figure S11. In-liquid AFM imaging of reconstituted bacterial membranes incubated with all-D NI01. Related to Figure 1 and Figure 2. (A) Topography of SLBs treated with D-NI01 (0.25 µM), with low-magnification (left) and high-magnification (right) images taken within the first 5 min of incubation. (B) A high-magnification image with height profiles as measured along the blue and white dashed lines. Colour bar is 15 nm, length scale bars are 500 nm for (A, left) and 100 nm for (A, right) and B.
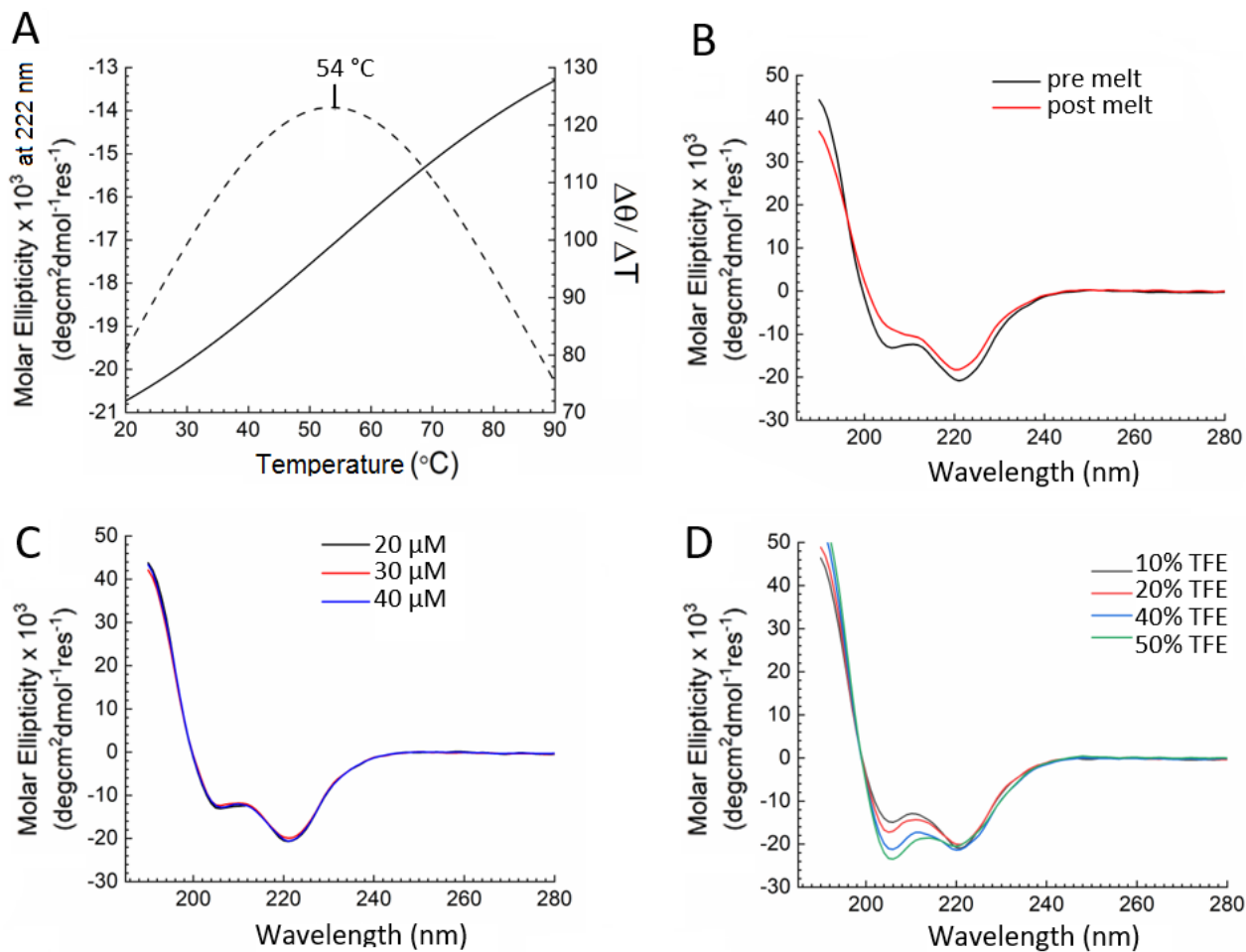
Figure S12. A53 folding. Related to Figure 5. (A) thermal unfolding curve and its first derivative highlighting a single transition point (T_M). CD spectra (B) recorded before (black line) and after (red line) thermal denaturation; (C) at different protein concentrations and (D) at varied TFE concentrations. Folding conditions: 20 µM protein, pH 7.4, 10 mM phosphate buffer, 20˚C.

Table S1. X-ray data collection and refinement statistics. Related to Figure 1.

	Native	Iodine soak	Native
Data collection			
Space group	$P\,2_12_12$	$P\,2_12_12$	$C222$
Cell dimensions (Å)	92.2, 117.9, 52.9	92.7, 117.6, 52.4	90.7, 99.4, 69.4
Resolution (Å)	46 – 1.69 (1.73-1.69)[§]*	93 – 2.10 (2.15-2.10)[§]	49-1.58 (1.62-1.58)[§]
R_{merge} (%)	5.8 (57.6)	11.3 (66.7)	5.4 (64.9)
$I\,/\,\sigma I$	14.1 (2.1)	15.4 (2.3)	18.3 (2.6)
Completeness (%)	99.0 (97.6)	96.8 (76.5)	99.9 (100)
Redundancy	4.4 (4.2)	10.6 (4.6)	6.4 (6.3)
Refinement			
Resolution (Å)	46-1.69		49-1.58
No. reflections	61,278		40,821
$R_{\mathrm{work}}\,/\,R_{\mathrm{free}}$	0.247/0.262		0.157/0.174
No. atoms			
Protein	3,374		1,706
Ligand/ion	40		10
Water	103		231
B-factors (Å^2)			
Protein	24.6		21.6
Ligand/ion	39.0		27.8
Water	26.4		36.5
R.m.s deviations			
Bond lengths (Å)	0.010		0.012
Bond angles (°)	1.47		1.70

*Values in parentheses are for highest-resolution shell.
[§]Data were collected from a single crystal

Table S2. Biological activities of NI01, its derivatives and other antimicrobial agents for comparison. Related to Figure 1.

| Cell | NI01 | | | α1α2 | α2α3 | α3α4 | α1α2α3 | α2α3α4 | ampicillin | melittin | polymyxin B |
	L-form	D-form	R-mutant								
	Minimum Inhibitory Concentration, μg/mL										
E. coli (ATCC 15597)	18	18	9	8	14	19	6	6	24	7	2
S. aureus (ATCC 6538)	5	5	5	8	>120	5	6	6	1	3	32
S. typhimurium (DA6192)	>300	>300	>300	32	>50	40	20	12	8	9	2
B. subtilis (ATCC 6633)	3	3	18	16	14	3	6	6	9	9	4
K. pneumoniae (NCTC 5055)	>300	>75	18	16	28	40	20	12	5	9	4
M. luteus (ATCC 49732)	2	2	2	3	2	9	6	3	1	2	2
P. aeruginosa (ATCC 27853)	>300	>300	>300	>140	14	>80	12	6	8	25	2
	HD_{50},[a] *μg/mL*										
Human erythrocytes	500	600	250	150	UD[b]	150	200	200	UD[b]	5	350

[a]median hemolytic doses to achieve 50% lysis; [b]undetectable

Table S3. Antibacterial activities of NI01 and its derivatives. Related to Figure 1.

| Cell | NI01 | | α1α2 | α2α3 | α3α4 | α1α2α3 | α2α3α4 |
	L-form	D-form					
	Minimum Inhibitory Concentration, μg/mL						
EMRSA (12817)	4	4	4	>128	4	32	16
EMRSA (12845)	4	4	2	>128	4	32	16
EMRSA (12873)	4	8	4	>128	4	32	16
E. coli (SBS363)	8	8	1	8	4	4	4
E. coli (ML35)	64	64	8	32	32	64	32

TRANSPARENT METHODS

Polypeptide Synthesis, Identification and Purification. NI01 and all its derivatives were assembled in a Liberty microwave peptide synthesizer (CEM Corp.) using Fmoc/^{t}Bu synthesis protocols with DIC/Oxyma as coupling reagents. NI01 and all-D NI01 were assembled on Fmoc-Ala-Wang resin and Fmoc-D-Ala-Wang resins, respectively. Both proteins were capped at their N-termini using p-nitrophenylformate. All the hairpins were synthesized as C-terminal amides on a Tentagel S RAM resin, leaving the N-termini uncapped. NI01, D-NI01, R-NI01, A53 and h1 were cleaved and deprotected using cleavage mixture A (94% TFA, 2% TIS, 2% DODT, 2% H_2O). For all the others a mixture B (95% TFA, 2.5% TIS, 2.5% H_2O) was used. NI01, D-NI01 and A53 were formylated at their N-termini. All peptides were then purified by semi-preparative RP-HPLC. The purity and identities of NI01 and derivatives were confirmed by analytical RP-HPLC ($\geq$95%) and MALDI-ToF mass-spectrometry:

MS [M + H]$^+$: NI01 – m/z 6072.3 (calc.), 6072.8 (found); D-NI01 – m/z 6072.3 (calc.), 6073.5 (found); R-NI01 – m/z 6314.4 (calc.), 6316.3 (found); A53 – m/z 6012.5 (calc.), 6013.6 (found); α1α2 – m/z 2773.4 (calc.), 2772.8 (found); α2α3 – m/z 2383.8 (calc.), 2384.0 (found); α3α4 – m/z 3149.7 (calc.), 3150.8 (found); α1α2α3 – m/z 3964.8 (calc.), 3964.8 (found); α2α3α4 – m/z 4263.0 (calc.), 4263.8 (found).

Analytical and semi-preparative RP-HPLC was performed on a Thermo Scientific Dionex HPLC System (Ultimate 3000) using a Vydac C18 analytical and semi-preparative (both 5 μm) columns. Analytical runs used a 10-70% B gradient over 30 min at 1 mL/min, semi-preparative runs were optimised for each peptide, at 4.5 mL/min. Detection was at 280 and 214 nm. Buffer A and buffer B were 5% and 95% (v/v) aqueous CH_3CN containing 0.1% TFA.

Crystal structure determination. Crystals of NI01 were obtained in two different forms, *P2₁2₁2* and *C222*, and diffraction data were collected to resolutions of 1.69 and 1.58 Å, respectively (Table S1). NI01 was obtained in two different crystal forms. The structure of the *P2₁2₁2* crystal form was solved by SIR using phasing from iodide ions. The asymmetric unit (AU) contains 8 NI01

molecules, arranged in 222 symmetry (Fig 1B); an individual NI01 structure was used to solve the *C222* crystal form, which has 4 molecules in the AU. Some of the intramolecular contacts between monomers are preserved between the two crystal forms.

Crystals were grown by sitting drop vapor diffusion at 20 ºC: equal volumes (200 nL) were mixed of protein and a reservoir solution of either 0.2 M aq. $(NH_4)_2SO_4$, 0.1 M aq. $CH_3COO^-Na^+$ (pH 4.5), 28% PEG, 2000 MME (*P2₁2₁2* crystal form) or 0.2 M aq. Li_2SO_4, 0.1 M aq. $CH_3COO^-Na^+$ (pH 4.5), 24% PEG 8000 (*C222* crystal form). Native crystals were cryoprotected by addition of glycerol to 20% (v/v) to liquor from a sitting drop well (all components therefore are at 80% of initial concentrations). Phasing was obtained from soaking of a single *P2₁2₁2* crystal in 0.4 M KI/20% glycerol. The crystal started to dissolve at this KI concentration, but exposure was sufficient to allow recovery with I⁻ ions incorporated. Data were collected at the Diamond Light Source (National Synchrotron Facility, Oxford, UK), using the following beamlines and wavelengths: native *P2₁2₁2* DLS IO4 (1.0725Å); KI derivative *P2₁2₁2* DLS I04 (1.5000Å); native *C222* DLS I04-1 (0.9200Å). Data were processed using XDS (Kabsch, 2010) from within the xia2 system for automated data reduction (Winter, 2010). Space-group assignment was assisted using POINTLESS (Evans, 2006). The KI dataset gave an anomalous slope of 1.13; 28 iodine sites were located using SHELX (Sheldrick, 2008) and subsequently phased using BP3 (Pannu et al., 2011) from within CCP4 suite (Collaborative Computational Project, Number 4, 1994) to give an FOM of 36% to 2.10Å. Electron density maps were improved using SOLOMON (Abrahams and Leslie, 1996) and a near-complete model for eight separate chains built using BUCCANEER (Cowtan, 2006). The model was completed by minor manual rebuilding using COOT (Emsley et al., 2010) and refinement using REFMAC (Murshudov et al., 1997). The *C222* crystal form was solved with a monomer from chain A of the *P2₁2₁2* crystal form, using PHASER (McCoy et al., 2007) as implemented within PHENIX (Adams et al., 2010), followed by automated model building and refinement in PHENIX. The final structures contained no Ramachandran outliers. Stereochemical parameters for both structures were examined using PROCHECK (Laskowski et al., 1993) and

were within or better than the tolerance limits expected for each structure at the resolution limits given in Table S1.

Lipid Vesicle Preparation. 1-palmitoyl-2-oleoyl-glycero-3-phosphocholine (POPC) with 1-palmitoyl-2-oleoyl-sn-glycero-3-phospho-(1'-rac-glycerol) (POPG) lipids used for vesicle construction were from Avanti Polar Lipids (Alabaster, USA). POPC was used as mammalian model membranes, and POPC/POPG (3:1, molar ratios) was used as bacterial model membranes. The lipids were weighted up, dissolved in chloroform-methanol (2:1, vol/vol), and dried under a nitrogen stream to form a thin film. The film was hydrated in 10 mM phosphate buffer (pH 7.4), vortexed for 2 min and bath sonicated for 30 min. The obtained suspension was extruded using a hand-held extruder (Avanti Polar lipids) (29 times, polycarbonate filter, 0.05 μm) to give a clear solution of small unilamellar vesicles, which were analysed (50 nm) by photon correlation spectroscopy (ZEN3600; Malvern Instruments, UK) following the re-suspension of vesicles to a final concentration of 1 mg/mL. Dynamic light scattering batch measurements were carried out in a low volume disposable cuvette at 25 °C. Hydrodynamic radii were obtained through the fitting of autocorrelation data using the manufacturer's Dispersion Technology Software (version 5.10).

Dynamic Light Scattering. Zetasizer Nano (ZEN3600, Malvern Instruments, UK) was used to measure size distributions and ζ-potential in low volume disposable cuvettes and folded capillary cells, respectively. The measurements were performed at 25 °C for NI01 (900 μM) in 10 mM phosphate buffer (pH 7.4). Hydrodynamic radii and ζ-potential values were obtained through the fitting of autocorrelation data using the manufacture's software, Zetasizer Software (version 7.03). The ζ-potential value reported is a mean of three independent measurements, with each measurement consisting of 10 recordings. Size distributions represent a mean of three independent measurements, with each measurement consisting of 20 recordings.

Circular Dichroism Spectroscopy. Aqueous peptide solutions (300 μL, at a given concentration) were prepared in filtered (0.22 μm), 10 mM phosphate buffer, pH 7.4. CD spectra recorded in the presence of synthetic membranes are for L/P molar ratio of 100. All CD spectra were recorded on

a JASCO J-810 spectropolarimeter fitted with a Peltier temperature controller. All measurements were taken in ellipticities in mdeg and converted to molar ellipticities by normalizing for the concentration of peptide bonds and cuvette path length ([θ], deg cm^2 dmol^{-1} res^{-1}). The data collected with a 1 nm step and 1 s collection time per step are presented as the average of 4 scans. Thermal denaturation curves were recorded with 2 °C intervals using 1 nm bandwidth, 180 s equilibration time for each spectrum and with 2 °C/min ramp rate.

Isothermal Titration Calorimetry. Measurements were obtained using a Microcal isothermal titration calorimeter-200 (ITC-200) which has a cell volume of ~ 0.2026 mL and a syringe volume of ~ 0.04 mL. The titrations were performed with a 60-s initial delay and a 120-s equilibration time between the start and end of each titration. Experiments were performed at 30 °C with a stirring speed at 750 rpm until no further enthalpy changes were observed. Binding isotherms were recorded for NI01 (500 μM, 38 injections of 1 μL each) titrated into lipid vesicles (380 μM, total lipid) in the cell. The observed heats were corrected for dilution effects by titrating the protein into the buffer. All data were corrected for the volume of the added titrant and analysed by proprietary software (Microcal Origin 7.0) using one-set binding model to allow for the determination of association constants (Ka), changes in enthalpy (ΔH) and entropy (ΔS). Each experiment was performed in duplicate.

Preparation of SLBs for in-liquid AFM imaging. SLBs were formed using a vesicle fusion method as described elsewhere (Lin et al., 2006). Freshly prepared vesicles (1.5 μL, 3 mg/mL) were added to cleaved mica that was pre-hydrated in 20 mM MOPS, 120 mM NaCl, 20 mM MgCl$_2$ (pH 7.4). After incubation over 45 min, the samples were washed 10 times with imaging buffer (20 mM MOPS, with 120 mM NaCl, pH 7.4) to remove unfused vesicles. The resulting SLBs were checked to confirm they were defect free. Mica discs (Agar Scientific, Stansted, UK) were glued to a metal puck, and freshly cleaved prior to lipid deposition.

In-liquid AFM imaging of SLBs. The topographic imaging of SLBs in aqueous buffers was performed on a Multimode 8 AFM system (Bruker AXS, USA) using Peak Force Tapping^{TM} mode

and MSNL-E cantilevers (Bruker AFM probes, USA). Images were taken at the PeakForce frequency of 2 kHz, PeakForce amplitude of 10-20 nm and PeakForce set-point of 10-30 mV (<100 pN). The images were then processed using Gwyddion (http://gwyddion.net) for line-by-line background subtraction (flattening) and plane fitting. NI01 or its derivatives were introduced into a 100-µL fluid cell (Bruker AXS, USA) to the final concentrations stated.

Minimum Inhibitory Concentrations assay. Minimum inhibitory concentrations (MICs) were determined by broth microdilution on *P. aeruginosa*, *E. coli*, *S. aureus*, *M. luteus*, *B. subtilis*, *S. typhimurium* and *K. pneumoniae* according to the Clinical and Laboratory Standards Institute. Typically, 100 µL of $0.5–1 \times 10^6$ CFU per ml of each bacterium in Mueller Hinton media broth (Oxoid) were incubated in 96-well microtiter plates with 100 µL of serial two-fold dilutions of the corresponding antimicrobial agent (from 100 to 0 µM) at 37 °C on a 3D orbital shaker. The absorbance was measured after the addition of NI01, its derivatives or an antibiotic at 600 nm using a SpectraMax i3x Multi-Mode Microplate Reader (Molecular Devices). MICs were defined as the lowest protein concentration that inhibited visible bacterial growth after 24 h at 37 °C. All tests were done in triplicate and results are summarized in Tables S2 and S3.

Hemolysis assay. Hemolysis was determined using human erythrocytes sourced commercially from Cambridge Bioscience Ltd. and used within two days. 10% (vol/vol) suspensions of human erythrocytes were incubated with NI01, its derivatives or antibiotics. The cells were rinsed four times in 10 mM phosphate buffer saline (PBS, Gibco™), pH 7.2, by repeated centrifugation and re-suspension (3 min at $3000 \times$ g). The cells were then incubated at room temperature for 1 h in either deionized water (fully hemolysed control), PBS, or with a corresponding antimicrobial agent in PBS. After centrifugation at $10,000 \times$ g for 5 min, the supernatant was separated from the pellet, and the absorbance was measured at 550 nm using a SpectraMax i3x Multi-Mode Microplate Reader (Molecular Devices). Absorbance of the suspension treated with deionized water defined complete hemolysis. All tests were done in triplicate and results are shown in Table S3. The values

given in Table S2 correspond to concentrations needed to lyse half of the sample population (50% lysis of erythrocytes) and are expressed as median hemolytic doses – HD_{50}.

References

Abrahams, J. P., and Leslie, A. G. W. (1996). Methods used in the structure determination of bovine mitochondrial F1 ATPase. Acta Crystallogr. D Biol. Crystallogr. 52, 30-42.

Adams, P. D., Afonine, P. V., Bunkoczi, G., Chen, V. B., Davis, I. W., Echols, N., Headd, J. J., Hung, L.-W., Kapral, G. J., Grosse-Kunstleve, R. W. et al. (2010). PHENIX: a comprehensive Python-based system for macromolecular structure solution. Acta Crystallogr. D Biol. Crystallogr. 66, 213-221.

Collaborative Computational Project, Number 4. (1994). The CCP4 Suite: Programs for protein crystallography. Acta Crystallogr. D Biol. Crystallogr. 50, 760-763.

Cowtan, K. (2006). The Buccaneer software for automated model building. 1. Tracing protein chains. Acta Crystallogr. D Biol. Crystallogr. 62, 1002-1011.

Emsley, P., Lohkamp, B., Scott, W. G., and Cowtan, K. (2010). Features and development of Coot. Acta Crystallogr. D Biol. Crystallogr. 66, 486-501.

Evans, P. (2006). Scaling and assessment of data quality. Acta Crystallogr. D Biol. Crystallogr. 62, 72-82.

Kabsch, W. (2010). XDS. Acta Crystallogr. D Biol. Crystallogr. *66*, 125-132.

Laskowski, R. A., McArthur, M. W., Moss, D. S., and Thornton, J. M. (1993) PROCHECK: a program to check the stereochemical quality of protein structures. J Appl. Crystallogr. 26, 283-291.

McCoy, A. J., Grosse-Kunstleve, R. W., Adams, P. D., Winn, M. D., Storoni, L. C., and Read, R. J. (2007). Phaser crystallographic software. J Appl. Crystallogr. 40, 658-674.

Murshudov, G. N., Vagin, A. A., and Dodson, E. J. (1997). Refinement of Macromolecular Structures by the Maximum Likelihood Method. Acta Crystallogr. D Biol. Crystallogr. 53, 240-255.

Pannu, N. S., Waterreus, W.-J., Skubak, P., Sikharulidze, I., Abrahams, J. P., and de Graaff, R. A. G. (2011). Recent advances in the CRANK software suite for experimental phasing. Acta Crystallogr. D Biol. Crystallogr. 67, 331-337.

Sheldrick, G. (2008). A short history of SHELX. Acta Crystallogr. A 64, 112-122.

Winter, G. xia2: an expert system for macromolecular crystallography data reduction. (2010). J Appl. Crystallogr. 43, 186-190.